Aerodynamic Analysis of Mathematically Modelled Propeller for Small UAV Using CFD in Different Temperature Conditions

Tamilselvan Ganesan,* – Niresh Jayarajan

PSG College of Technology, Department of Automobile Engineering, India

Unmanned aerial vehicle (UAV) usage has witnessed a significant rise owing to its cost-effectiveness and versatile applications. However, the design techniques for UAV propellers, encompassing aerodynamic and structural analysis, have received limited attention from researchers. A well-designed propeller can effectively reduce battery consumption and enhance overall efficiency. This study focuses on mathematically designed propellers and compares them with advanced precision composite (APC) Slow Flyer propeller blades in terms of thrust coefficients, power coefficients, and efficiency. The investigation includes the utilization of tetrahedron meshing in simulations, employing the standard k–ω (k–omega) model. To evaluate the accuracy of the blade element theory (BET) in predicting thrust, the simulation data is compared with BET results. Furthermore, the study encompasses experimental testing to validate the simulation findings. The findings demonstrate that the mathematically modelled propeller outperforms the APC Slow Flyer propeller across all ranges of revolutions per minute (rpm). When comparing the results of both methods, BET exhibits an error difference of 10 % in higher rpm ranges, but this error diminishes as the rpm decreases. This study contributes a novel design technique for modelling propellers using mathematical formulas and provides a comprehensive comparison of their aerodynamic properties with existing propellers, utilizing both BET and computational fluid dynamics (CFD) methods, along with experimental validation.
Keywords: unmanned aerial vehicle, propeller, computational fluid dynamics, blade element theory, mathematical design

Highlights
- *Design the propeller based on the mathematical model generated using the Eppler E63-based airfoil due to the amount of lift it generates to increase the UAV thrust and efficiency.*
- *Perform the CFD analysis for these propellers in various temperature conditions and generate the results.*
- *Compare the designed propeller with the APC Slow Flyer, which is among the most commonly used in 10' UAV propellers.*
- *Blade element theory has been used to verify the results generated from the analysis and noted the error difference between these two.*

0 INTRODUCTION

Unmanned aerial vehicles (UAVs) play a vital role in defence missions, encompassing remote sensing, surveillance, and data collection in challenging environments with varying temperatures [1]. The lifespan of a drone is crucial in such missions, as numerous operational factors significantly impact its performance and structural integrity [2] to [4]. Rotor blades serve as fundamental components of drones and most UAVs, with operational temperature being a crucial parameter in their design. However, a comprehensive database on UAV performance in harsh environmental conditions is still lacking, which is critical for evaluating battery lifespan and thrust prediction in relation to weather conditions. Our primary objective is to gather data on propeller performance under cold temperatures for preliminary research on the impact of environmental factors on UAV propulsion systems [5] to [9].

In recent years, several experiments have been conducted on small UAVs and their power systems. Brandt and Selig [10] focused on propellers for small unmanned aerial vehicles, creating a reference database that emphasizes thrust generation in windy conditions and propeller behaviour in low Reynolds flow conditions. Scanavino et al. [11] proposed a comparison between blade element theory and experimental results obtained from extreme weather conditions using a 15' × 5' carbon fibre propeller. Another significant contribution was made by Russell et al. [12], who analysed the performance of five commercial UAVs in a wind tunnel under static conditions, providing a comprehensive overview of their overall performance. That article includes information about the experimental analysis, test matrix, and results obtained from laser scanner measurements. However, when it comes to UAVs in harsh environments, few papers describe the performance of these vehicles. Precision Hawk [13] conducted environmental experiments on multi-rotor and fixed-wing propellers in partnership with the Automotive Centre of Excellence. Unfortunately, no experimental data from these studies have been made available for investigation. More recently, research on propellers has focused on ice accretion conditions

[14] to [17], exploring the aerodynamic performance of propellers at various water content and operational temperature levels. The goal of this characterization was to develop a new anti-ice propeller component that would reduce power consumption. A passive solution based on surface wettability and hydrophobic materials has been proposed.

The UAV industry has only recently begun providing end users with information on flying recommendations in extreme circumstances [18] and [19]. For instance, the Alta 8 flying handbook by Freefly Systems includes a table that shows the maximum take-off weight as a function of temperature and altitude. However, beyond conventional flying conditions, data are often based on projections, real-world experiments, and user input.

In our research, we focus on designing propellers using numerical formulas to optimize their efficiency. We specifically employ high lift, low drag airfoils that are well-suited for low Reynolds numbers, such as the Eppler E63 airfoil. By utilizing the airfoil's data coordinates and implementing a spline interpolation technique, we design propellers based on these numerical values using computer aided design (CAD) software. Subsequently, the propellers undergo comprehensive analysis of various aerodynamic properties, including thrust, lift, and drag, through the utilization of computational fluid dynamics (CFD) simulations. To ensure controlled conditions, we employ a specialized climate-controlled facility to collect precise experimental data. The experimental results are then compared with the CFD simulations, as well as benchmarked against industry-leading propellers such as the 10' APC propeller and the classic NACA 4412 propeller. By combining both experimental and computational approaches, our primary objective is to provide a comprehensive analysis of the performance of these mathematically designed propellers.

1 ENVIRONMENTAL CONDITIONS

Testing the propeller in harsh environmental conditions is one of this experiment's main objectives. Propeller thrust data will be useful for UAV objectives and will increase reliability while flying in extreme environmental conditions. For this experiment, the pressure is kept constant during propeller testing in various temperature environments. The temperature of the environment influences air density called the isobaric test as shown in Table 1.

Table 1. *Isobaric test conditions*

Temperature [ºC]	Pressure [hPa]	Air density [kg/m³]
42.5	989	1.0924
33.3	990	1.1256
29.3	990	1.1405
24.8	990	1.1577
18.1	983	1.1760
-13.5	978	1.3124
-20.3	978	1.3477
-25.7	978	1.3771
-28.4	977	1.3909
-34.5	974	1.4221

2 DESIGN OF PROPELLER

2.1 Design of Optimal Rotor Blades

The rotation of a propeller blade creates turbulence, which reduces its efficiency. To maintain balance and maximize efficiency, propellers are typically designed with two blades. Adding more blades brings diminishing returns as the blades become
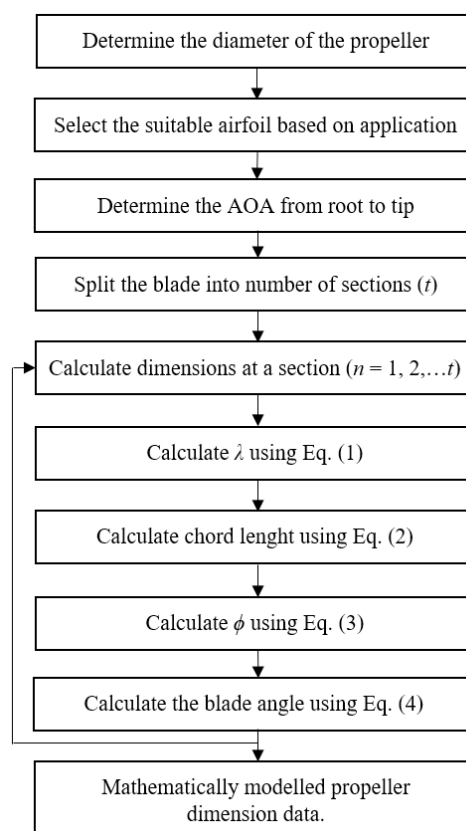
Fig. 1. *Methodology*

closer together, further decreasing efficiency. While a tri-blade or quad-blade configuration can provide additional thrust, the benefits are less pronounced. Therefore, most propellers used in small UAVs have two blades. In this research, a 10' propeller is chosen as it is widely used in small UAV applications. To enhance accuracy, each blade of the propeller is divided into 18 sections, resulting in a total of 32 sections for the complete propeller design. This segmentation allows for precise control over chord length and blade angle at each section. The propeller models are created using a set of formulas that define parameters such as chord length, tip speed ratio, air flow angle, and blade angle. The propellers are modelled in methods as shown in Fig. 1. These formulas ensure the propeller is designed with optimal characteristics for efficient performance.

The tip speed ratio (TSR), denoted as λ, represents the ratio of the tangential speed of the propeller blade tip to the wind velocity. It is a crucial parameter in propeller design as it directly influences various aspects of performance. When the tip speed increases, it can result in increased noise generation and vibrations within the propeller system. The formula for calculating the tip speed ratio is expressed in Eq. (1) as follows:

$$\lambda = \frac{Blade\ tip\ speed}{Wind\ speed} = \frac{\omega \cdot r}{v}, \qquad (1)$$

where ω is rotational speed [rad/s], r radius at the point of computation [m], R radius at the tip [m], and v wind velocity [m/s].

The chord length of a propeller refers to the distance between its leading and trailing edges in the direction of the wind. Increasing the chord length of a propeller can lead to improved efficiency. This is because a propeller with a larger width offers a larger surface area for interaction with the air. According to Newton's Third Law, a propeller can push back a greater number of air particles in a single rotation, resulting in a greater reaction force that propels the vehicle forward. Therefore, increasing the chord length contributes to enhanced propeller performance [20]. The calculation of the chord length is determined by utilizing Eq. (2) as follows:

$$Chord\ length = \frac{5.6 \cdot R^2}{\left(2 \cdot Cl \cdot r \cdot \lambda^2\right)}. \qquad (2)$$

The inflow angle is the angle formed between the axis of the propeller and the direction of the airstream. It plays a significant role in the propeller equation

[21]. The equation for determining the inflow angle Eq. (3) as follows:

$$\phi = tan^{-1}\frac{2}{3\lambda}. \qquad (3)$$

The blade angle is the angle between the chord of the propeller blade and the plane of rotation. It is measured at a specific position along the length of the blade. The blade angle is the sum of the inflow angle and the angle of attack of the propeller, as stated in Eq. (4). To maintain a relatively constant angle of attack (AOA) along the length of the blade, the propeller blade twists along its length. This twist is necessary because the blade speed is significantly higher at the tip compared to the base.

$$Blade\ angle\ =\ Inflow\ angle\ +\ Angle\ of\ attack. \qquad (4)$$

2.2 Reverse Engineering the APC and NACA Propellers

The APC Slow Flyer 10' propellers are widely used in small UAVs and are manufactured by APC. They are two-bladed propellers that have become popular in the UAV industry. Another commonly used propeller in the past is the NACA 4412 propeller. Both propellers have a diameter of 0.254 m and a fixed pitch.
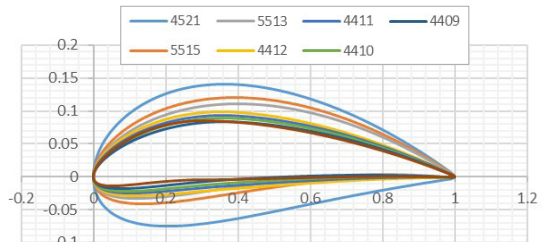
Fig. 2. *Sectional airfoil structures of APC*

The APC propeller incorporates a combination of NACA 4 and 5 series airfoils, as depicted in Fig. 2, while the NACA 4412 propeller is based on a single airfoil bearing its name. To obtain detailed information about the propeller profiles, a 3D scanner called ATOS 2M was used. This scanner can capture the product part in the form of images or drawings, a process known as 'reverse engineering'. The scanning process involves mounting the scanner on a tripod for scanning large parts, or it can be operated manually. By obtaining a reference point from the rotating table, the entire propeller is scanned. The scanned blade profiles of the APC and NACA propellers were exported to IGES format, providing valuable data as shown in Fig. 3. The three distinct designs of

Table 2. *Propeller design parameters for E63 airfoil*

S. No	r / R	Tip speed ratio	In flow angle	Chord length [mm]	Angle of attack	Blade angle
1	0.10	0.754	35.338	18.495	5.60	40.938
2	0.20	1.508	22.376	17.826	5.04	27.416
3	0.25	1.885	18.638	17.318	4.76	23.398
4	0.30	2.262	15.906	15.838	4.48	20.386
5	0.35	2.639	13.841	15.181	4.20	18.040
6	0.40	3.016	12.234	14.998	3.92	16.155
7	0.45	3.393	10.952	13.898	3.64	14.592
8	0.50	3.770	9.908	13.367	3.36	13.268
9	0.55	4.147	9.042	12.611	3.08	12.122
10	0.60	4.524	8.313	11.806	2.80	11.113
11	0.65	4.901	7.691	11.647	2.52	10.215
12	0.70	5.278	7.155	11.032	2.24	9.395
13	0.75	5.655	6.688	10.674	1.96	8.648
14	0.80	6.032	6.278	10.378	1.68	7.958
15	0.85	6.409	5.914	10.323	1.40	7.314
16	0.90	6.786	5.591	10.533	1.12	6.711
17	0.95	7.163	5.300	10.093	0.84	6.140
18	1.00	7.540	5.038	9.697	0.56	5.598
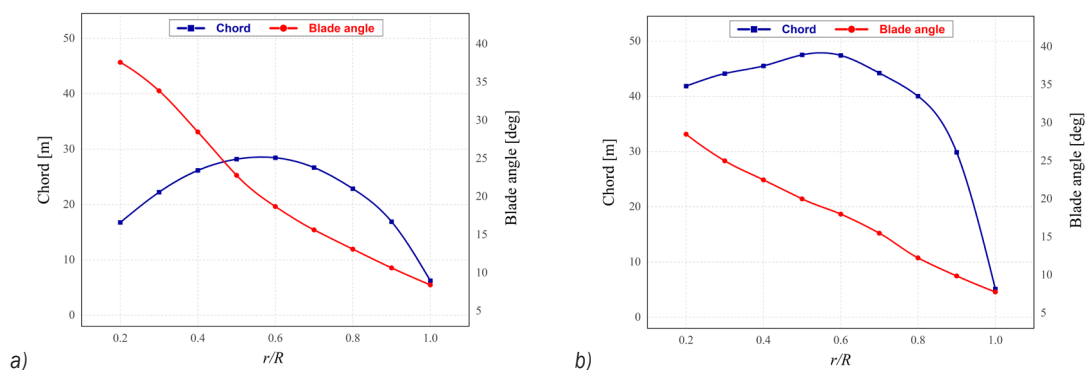
Fig. 3. *Data from ATOS 2M: Chord and blade angle of: a) APC propeller, and b) NACA 4412 propeller*

Fig. 4. a) *Mathematically modelled E63 propeller, b) APC Slow Flyer, and c) NACA 4412 propeller*

propellers as shown in Fig. 4 are made using the CAD design software.

3 TURBULENCE SIMULATION MODEL

3.1 Selection of Flow Domain

The flow region and numerical predictions were conducted using ANSYS software. The design CAD models were imported into ANSYS Fluent, where the geometry was created. To ensure accurate simulations, a domain was built around the propeller that extended taller than the propeller itself. This was done to prevent the wall boundary, which is closer to the propeller, from heating up quickly due to the airflow generated during propeller rotation. Additionally, the domain was carefully chosen to avoid any recirculation within the domain, as recirculation can introduce variations

in the results. The domain boundary was extended higher than normal and designated as the rotating domain, as illustrated in Fig. 5. A static environment was created around this rotating domain. Before commencing the simulation, the geometry was prepared with the appropriate environment settings, including airflow conditions and Boolean operations for specific regions.
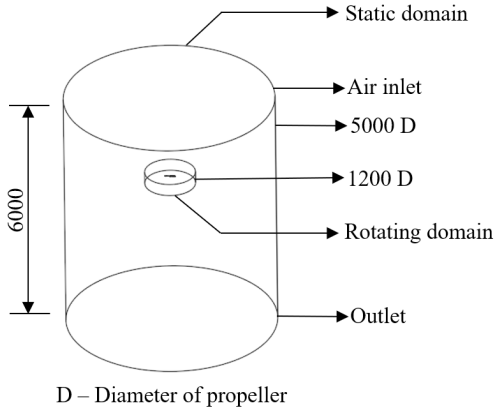

Fig. 5. *Flow domain dimensions in [mm]*

3.2 Mesh Generation and Dependency Test

Mesh generation must ensure high-quality meshes that balance calculation accuracy and computation time. If the element size of the mesh is too large, the solution's final precision will be compromised. Conversely, if the element size is too small, the computation time will significantly increase. Therefore, an optimal element size must be determined to achieve accurate and efficient simulations. Initially, the computational domain was aligned using a line surface-to-body sequence. Given the large size of the propeller surface and its curvature, efforts were made to reduce curvature effects, particularly through surface splitting and merging techniques.

A mesh dependency study was conducted in the CFD simulation to determine an appropriate mesh size. The study focused on evaluating thrust and drag. Fig. 6 illustrates that consistent results were obtained with a mesh consisting of more than 2.5 million elements. To accurately capture the behaviour of the viscous sub-layer, mesh refinement was applied to all sides of the rotating domain, which was constructed around the propeller blade boundaries. The boundary criterion was determined by selecting the appropriate named selection for the primary part. Table 3 provides details of the node and element sizes for the propeller. Furthermore, Fig. 7 showcases the computational domain and the results of the meshing process. To

achieve better simulation results, tetrahedral meshes were employed for both the propeller and its rotating domain. The mesh size of the rotating domain was intentionally kept smaller than that of the static domain, which served as a boundary wall. Proper naming conventions were applied to all faces and domains using named selections to ensure clarity and organization throughout the simulation process.
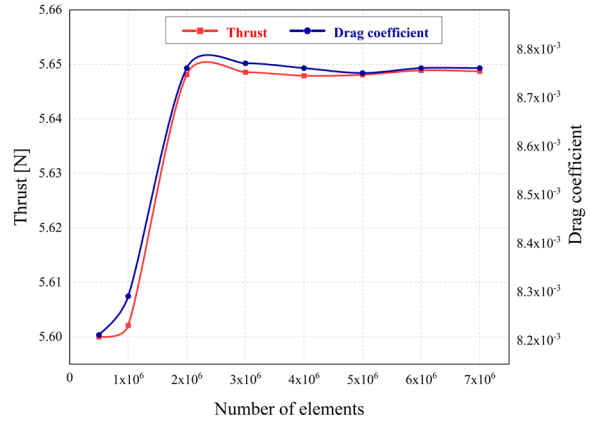

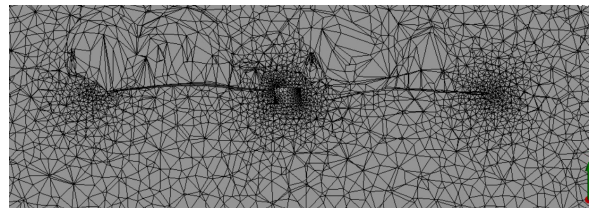**Fig. 6.** *Results of CFD mesh dependency test*

Fig. 7. *Tetrahedron mesh generation*

Table 3. *Mesh size of each propeller*

Propeller	Node	Element
E63	451628	3215652
NACA	452587	3368426
APC	458564	3224153

3.3 Turbulence Model Properties

The CFD simulation involved three distinct blade rotation speeds: 4000 rpm, 6000 rpm, and 6500 rpm. The free stream velocity was determined at the intake boundary, while the outflow was set at the outlet boundary. All walls within the domain were assigned as non-slip boundaries. Turbulence modelling played a crucial role in achieving accurate simulation results, and six different turbulence models were considered. The selection of the turbulence model was based on its ability to closely match experimental data. The chosen turbulence model in this investigation was the

k-omega normal model, which exhibited the lowest percentage difference compared to the other models (1.1249 %). The k–omega turbulence model is widely used to capture the effects of turbulent flow conditions and belongs to the Reynolds-averaged Navier-Stokes (RANS) family of turbulence models. It involves solving two transport equations for turbulent kinetic energy (k) and turbulent dissipation rate (omega). These equations account for historical effects such as convection and turbulent energy diffusion, providing a comprehensive representation of turbulence.

Kinetic energy equation:

$$\frac{\partial}{\partial t}\left(\rho k\right) + \frac{\partial}{\partial x_j}\left(\rho u_j k\right) = \rho \tau_{ij} \frac{\partial u_i}{\partial x_j} - \beta \rho k \omega +$$
$$\frac{\partial}{\partial x_j}\left[\left(\mu + \sigma \frac{\rho k}{\omega}\right) \frac{\partial k}{\partial x_j}\right]. \tag{5}$$

Specific dissipation rate:

$$\frac{\partial}{\partial t}\left(\rho \omega\right) + \frac{\partial}{\partial x_j}\left(\rho u_j \omega\right) = \alpha \frac{\omega}{k} \rho \tau_{ij} \frac{\partial u_i}{\partial x_j} - \beta \rho \omega^2 +$$
$$\sigma_d \frac{\rho \partial k \partial \omega}{\omega \partial x_j \partial x_j} + \frac{\partial}{\partial x_j}\left[\left(\mu + \sigma \frac{\rho k}{\omega}\right) \frac{\partial \omega}{\partial x_j}\right], \tag{6}$$

Table 4. *Simulation parameters*

Parameters	Values
Time	Transient
Time step	0.015
Number of Time Step	100
Max Iteration per time step	40
Viscous model	k–omega, Normal
Fluid medium	Air
Inlet velocity	15 m/s
Type of flow	Transient
Air density	1.225 kg/m³
Pressure-velocity coupling	Simple scheme
Gradient	Least squares cell based
Interpolating scheme (momentum)	Second-order upwind
Interpolating scheme (specific dissipation rate)	Second-order upwind

The k–omega model is particularly suitable for near-wall treatment and offers improved performance for complex boundary layer flows with adverse pressure gradients and separations, such as in external aerodynamics and turbomachinery applications. The simulation parameters used in the study are summarized in Table 4, ensuring the accuracy and reliability of the simulation results.

The simulation of the propeller employed a second-order upwind interpolation scheme. In computational physics, an upwind scheme is a discretization method used to solve hyperbolic equations and approximate the derivatives in a flow field. To better understand its function, let us consider the one-dimensional (1D) advection equation, Eq. (7). The advection equation is commonly used when analysing the movement of fluid through a passage.

1D advection equation:

$$\frac{\partial u}{\partial t} + a \frac{\partial u}{\partial x} = 0. \tag{7}$$

The advection equation represents the propagation of a wave with a specific velocity along the x-axis. It is commonly used to analyse one-dimensional linear advection. Let us consider a standard grid point i in a one-dimensional domain. In this domain, point 1 has two directions: towards the negative infinity side (upwind) and towards the positive infinity side (downwind). If the velocity is positive, the wave propagates towards the right side. In this case, the left side of point i is referred to as the upwind side, while the right side is called the downwind side. An upwind scheme is characterized by having a higher number of $\partial u / \partial x$ data points on the upwind side. In the case of the first-order upwind scheme, a 2-point grid data is used in the Taylor series approximation. However, the second-order upwind scheme employs a combination of 3-point backward difference and 3-point forward difference in the data points, as depicted in Eqs. (8) and (9). This method offers improved accuracy due to its reduced diffusivity compared to the first-order upwind scheme.

3-point backward difference:

$$u_x^- = \frac{3u_i^n - 4u_{i-1}^n + u_{i-2}^n}{2\Delta x}, \tag{8}$$

3-point forward difference:

$$u_x^+ = \frac{-u_{i+2}^n + 4u_{i+1}^n - 3u_i^n}{2\Delta x}. \tag{9}$$

4 RESULTS

4.1 Efficiency

CFD simulations were performed on three different propellers, namely the APC Slow Flyer, NACA 4412, and E63 designed propellers, under normal environmental conditions. The objective was to compare their respective efficiencies. In the CFD analysis, various parameters were calculated, including thrust generated T in [N], torque output Q in

[N·m], fluid density ρ in [kg/m³], propeller speed n in [rpm], propeller diameter D in [m], and power P [W]. To evaluate the performance of the propellers, several coefficients were derived from the CFD data. These include the thrust coefficient C_T, torque coefficient C_Q, power coefficient C_P, advance ratio J, and efficiency η. These coefficients were computed using specific equations. The efficiency values for each propeller are presented in Table 5.

$$J = \frac{V}{nD}, \tag{10}$$

$$C_t = \frac{P}{\rho n^2 D^4}, \tag{11}$$

$$C_p = \frac{P}{\rho n^3 D^5}, \tag{12}$$

$$\eta = \frac{JC_t}{C_p}. \tag{13}$$

Table 5. *Efficiency comparison on various advance ratios*

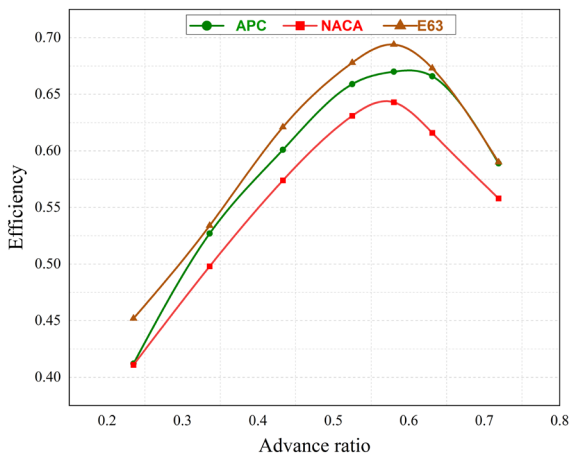| Advance ratio	Velocity [m/s]	APC η	NACA 4412 η	E 63 η
0.235	2.999	0.412	0.411	0.452
0.336	4.234	0.527	0.498	0.534
0.433	5.500	0.601	0.574	0.621
0.525	6.666	0.659	0.631	0.678
0.580	7.250	0.670	0.643	0.694
0.631	7.999	0.666	0.616	0.673
0.719	9.100	0.589	0.558	0.590

Fig. 8. *Propeller efficiency comparison between E63, NACA and APC propellers*

Fig. 8 depicts a comparison graph showcasing the efficiency of the three propellers. Notably, the propeller designed using the E63 airfoil exhibits a remarkable efficiency of nearly 70 % at an advance ratio of 0.58 before experiencing a decline. A common trend among all propellers is that their efficiency gradually decreases beyond the 0.58 advance ratio. In terms of initial efficiency, both the APC and NACA propellers demonstrate similar performance, but as the advance ratio increases, the APC propeller slightly outperforms the NACA propeller. In contrast, the NACA propeller, with its comparatively lower lift structure, exhibits the lowest efficiency among the three propellers. However, the propeller based on the E63 airfoil consistently maintains superior efficiency throughout the entire range. The high lift characteristics of the E63 airfoil contribute to its enhanced efficiency compared to the other two propellers.

4.2 Aerodynamic Numerical Solution

The numerical analysis of the three propellers focused on analysing their aerodynamic properties, including thrust, lift force, and drag coefficient. The analysis was conducted at various temperature settings and at three different speeds, resulting in a total of 30 simulations for each aerodynamic property. The analysis revealed that as the propeller speed decreases, both the thrust and lift force decrease as well. While this relationship may seem obvious, it is important to consider that thrust and lift force are directly proportional to the pressure acting on the propeller. The results clearly indicate that the propeller based on the E63 airfoil is less susceptible to pressure compared to the other two propellers, as illustrated in Fig. 9. This suggests that the mathematically modelled propeller exhibits superior efficiency compared to the other propellers. The thrust force generated by the propeller plays a crucial role in propelling a UAV through the air. It is responsible for overcoming the drag and weight of the drone, enabling it to maintain flight.

$$T = \dot{m} \cdot V, \tag{14}$$

where $\dot{m}$ is mass flow rate calculated as:

$$\dot{m} = \rho A V. \tag{15}$$

Substitute the Eq. (14) into Eq. (15), and we get

$$T = \rho A V^2. \tag{16}$$

Fig. 10 demonstrates the thrust generated by different propellers under various environmental conditions and at three rpm ranges. The simulation results clearly show that the mathematically designed E63 propeller outperforms both the NACA and APC propellers in terms of thrust. This superiority is due
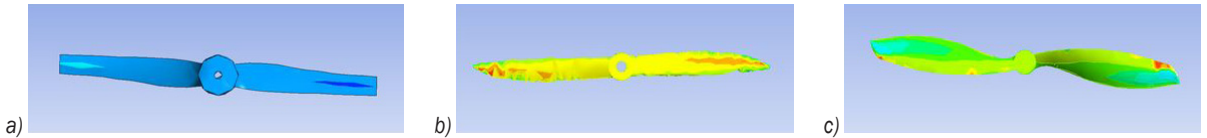
Fig. 9. *Pressure acting on the propeller at 6000 rpm*

to the E63 propeller's utilization of the high lift and low drag characteristics of its airfoil structure. Despite the NACA airfoil structure variations along the APC propeller sections, the mathematically designed propeller consistently exhibits better blade angle efficiency along its entire length. This efficiency advantage is particularly evident at 5000 rpm, where the E63 propeller generates nearly twice the thrust force compared to the APC propeller. In contrast, the NACA propeller performs poorly, producing less than 2 N of thrust. The increased efficiency of the E63 propeller results in reduced battery usage, as it generates more lift even at lower rpm ranges.
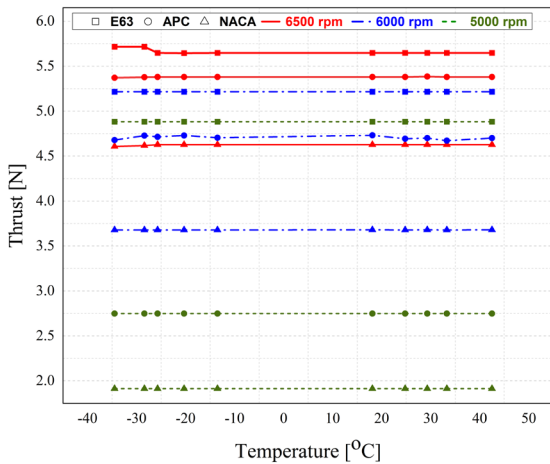

Fig. 10. *Thrust vs. temperature in three different rpms*

Drag on the propeller surface is caused by the velocity difference between the top and bottom portions. Aerodynamicists employ the drag coefficient to account for the complex relationships between geometry, angle, and flow conditions, which affect aircraft drag. The drag equation can be rearranged to solve for the drag coefficient in terms of other variables. From Fig. 11, it is evident that the APC propeller exhibits greater drag compared to the other two propellers. The APC propeller experiences high drag across all RPM ranges, primarily due to its utilization of a low lift airfoil structure at the tip. The propeller tip speed ratio being significantly higher than at the root contributes to the NACA series airfoil having higher drag coefficient values when compared

to the E63. Consequently, the APC propeller generates more drag than the other two propellers. When comparing these three propellers, the mathematically designed E63-based propeller demonstrates superior performance. The drag force can be calculated as half the product of the drag coefficient, air density, area, and the square of the velocity.

$$Drag \ force = \frac{1}{2}C_d \rho A V^2, \qquad (17)$$

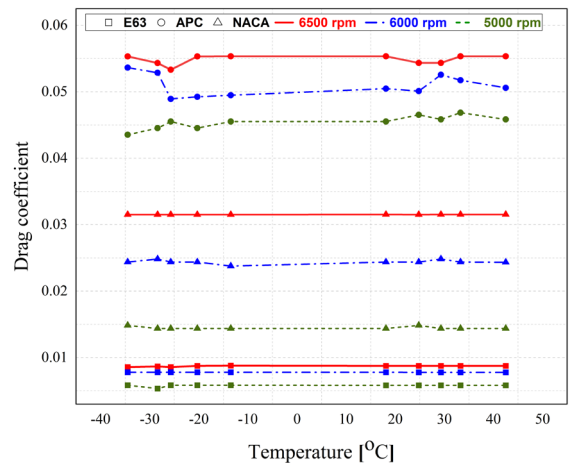where C_d is a drag coefficient, and A is area of propeller.

Fig. 11. *Drag coefficient vs. temperature in three different rpms*

Lift refers to the total force perpendicular to the incoming flow direction, whereas drag force runs parallel to the flow direction. Lift plays a crucial role in counteracting the force of gravity. From Fig. 12, it is evident that the E63 propeller performs exceptionally well at 6500 rpm. The APC propeller demonstrates a relatively closer lift force to the E63, but its performance diminishes due to the significant drag it generates at lower rpm, resulting in minimal lift production. In contrast, the NACA propeller performs poorly compared to the other two. This is primarily due to the inferior airfoil properties of the NACA 4412 in contrast to the superior characteristics of the E63. Overall, the E63 consistently outperforms both the APC and NACA propellers.
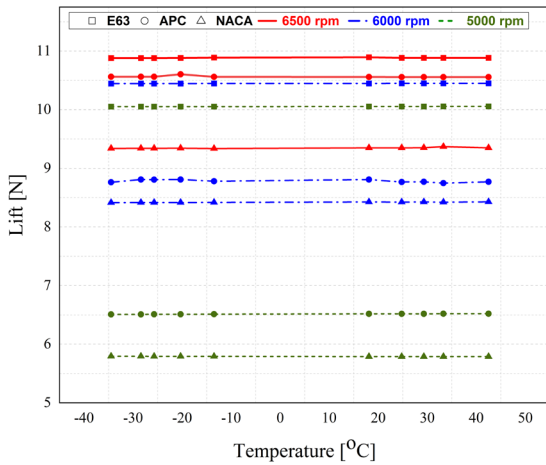
Fig. 12. *Lift force vs temperature in three different rpms*

4.3 Blade Element Theory

The BET offers the evaluation of propeller performance based on geometrical parameters, aerodynamic coefficients, and operating conditions [4], [22] to [24]. However, this theory overlooks secondary effects like tip vortex and radial flow, which can have a negative impact on total thrust output [25]. The distributions of airfoil profile, chord, and twist are represented as functions of the distance from the propeller hub using Eqs. (18) to (23). As the propeller profile varies, simulations were conducted using a simplified E63 airfoil for the mathematically designed propeller, NACA 4412 airfoil for the NACA propeller, and various NACA airfoils for different sections of the APC propeller. Comparison results between simulation and BET thrust force as shown in Fig. 13.

The angle between the thrust and lift directions is defined as

$$\varphi = \theta - \alpha. \quad (18)$$

The thrust of the blade section can be written as

$$\Delta T = \Delta L \cos \varphi - \Delta D \sin \varphi, \quad (19)$$

where

$$\Delta L = \frac{1}{2} C_L \cdot \rho A V^2 c \cdot dr, \quad (20)$$

$$\Delta D = \frac{1}{2} C_D \cdot \rho A V^2 c \cdot dr. \quad (21)$$

Therefore, the thrust equation becomes

$$\Delta T = \frac{1}{2} \rho A V^2 c (C_L \cos \varphi - C_D \sin \varphi) B \cdot dr. \quad (22)$$

To calculate the total thrust generated by the propeller for a specific rpm
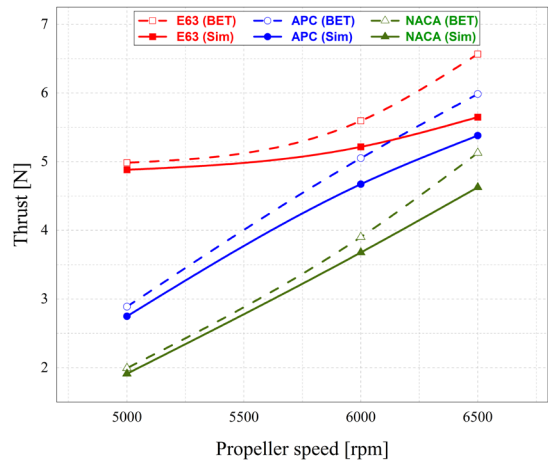
$$T = \Sigma \Delta T. \quad (23)$$

Fig. 13. *Thrust comparison between BET and SIM*

Comparisons were made between the experimental data and the results obtained from the blade element theory. The BET technique generally follows similar patterns, but it significantly overestimates the thrust force at higher rpm, with an error margin of approximately 10 % to 15 % compared to the actual results. This indicates that there are interactions between the propellers that are not accounted for in the basic coaxial model. However, both the CFD approach and the BET method yield similar thrust predictions when approaching lower rpm, with differences of less than 13 % between the simulated data and the blade element theory. Notably, the accuracy improves as the rotational speed decreases.

4.4 Experimental Ssetup

The experimental setup for propeller thrust calculation involves several components. Firstly, a weighing scale is utilized to measure the lifting force generated by the propeller. The motor responsible for rotating the propeller is securely mounted on a wooden structure. A servo controller is employed to regulate the 2200 kV brushless direct current (BLDC) motor speed and control its rotation. The motor is connected to a 30 A electronic speed controller (ESC) and is powered by a 3S battery. As the propeller rotates, it generates a lifting force that is transferred to the weighing scale. The scale readings are carefully observed and recorded. To convert the readings into Newtons, a

suitable conversion factor or calibration procedure is applied, allowing for accurate measurement of the propeller thrust. The setup image as shown in Fig. 14 and the result compare with the simulation values are tabulated in Table 6.
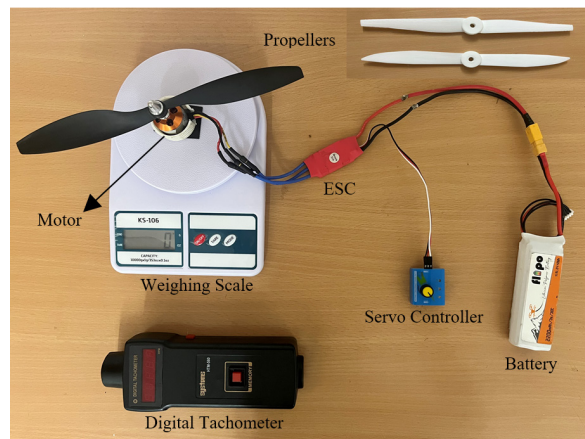

Fig. 14. *Experimental setup to test the thrust*

Table 6. *Error comparison of simulation thrust to the experimental values*

Propeller	rpm	Thrust (Sim)	Thrust (Exp)	Error [%]
E63	6500	5.548	5.165	6.90
	6000	5.216	4.868	6.67
	5000	4.881	4.562	6.53
APC	6500	5.380	4.963	7.75
	6000	4.672	4.325	7.42
	5000	2.749	2.552	7.16
NACA	6500	4.627	4.289	7.30
	6000	3.679	3.421	7.01
	5000	1.912	1.778	7.00

The E63 propeller, designed based on a mathematical model, was 3D printed using ABS material through the process of fused deposition modelling (FDM). The results of the comparison between the UAV 10' propeller, the novelty developed E63 airfoil structure-based mathematical modelled propeller, the NACA 4412 propeller, and the industry-leading APC Slow Flyer were obtained through both CFD simulation and experimental testing. The analysis revealed an error deviation ranging from 6.5 % to 7.7 % between the predicted and observed values. It was observed that the CFD simulations tended to overestimate the performance values compared to the theoretical predictions. However, it is important to note that the variation was not significantly large, and the results obtained from the CFD simulations were still reasonably comparable to the experimental data.

5 CONCLUSION

In conclusion, this research introduced a mathematical model for a UAV propeller, incorporating various airfoil structures. Experimental tests were conducted to evaluate the propeller's performance in terms of thrust, lift, and drag. The designed E63 propeller, utilizing the high lift E63 airfoil structure, exhibited superior characteristics compared to the APC propeller and the NACA 4412. It generated greater thrust, produced higher lift force, and experienced less drag. The APC propeller showed good performance at 6500 rpm but experienced a decline at lower speeds due to increased drag. The NACA propeller performed inadequately when compared to both the E63 and APC. The slight changes in aerodynamic properties observed at different temperatures had minimal impact on propeller performance. Comparisons with calculations from the BET showed satisfactory correlation at lower rpm ranges but increased errors at higher rpms. Nonetheless, the BET remains a valuable tool for preliminary propeller evaluation when the geometry is known. Overall, the mathematically designed propellers incorporating the high lift E63 airfoil structure consistently demonstrated superior performance across various temperature ranges in comparison to the other propellers tested.

6 REFERENCES

[1] A.M. Pérez, Lopez, O., Poroseva, S.V., Escobar, J.A. (2019). Computational study of a small rotor at hover using CFD and UVLM. *AIAA Scitech 2019 Forum*, **DOI:10.2514/6.2019-0597**.

[2] Goh, G.D., Agarwala, S., Goh, G.L., Dikshit, V., Sing, S.L., Yeong, W.Y. (2017). Additive manufacturing in unmanned aerial vehicles (UAVs): Challenges and potential. *Aerospace Science and Technology*, vol. 63, p. 140-151, **DOI:10.1016/j.ast.2016.12.019**.

[3] Kontogiannis, S.G., Ekaterinaris, J.A. (2013). Design, performance evaluation and optimization of a UAV. *Aerospace Science and Technology*, vol. 29, no. 1, p. 339-350, **DOI:10.1016/j.ast.2013.04.005**.

[4] Anemaat, W.A., Schuurman, M., Liu, W., Karwas, A.A. (2017). Aerodynamic design, analysis and testing of propellers for small unmanned aerial vehicles. *55th AIAA Aerospace Sciences Meeting*, **DOI:10.2514/6.2017-0721**.

[5] Kwon, H.I., You, J.Y. & Kwon, O.J. (2012). Enhancement of wind turbine aerodynamic performance by a numerical optimization technique. *Journal of Mechanical Science and Technology*, vol. 26, p. 455-462, **DOI:10.1007/s12206-011-1035-2**.

[6] Yoon, S., Nasa, Diaz, P.V., Boyd, D.D., Chan, W.M., & Theodore, C.R. (2017). Computational Aerodynamic Modeling of Small Quadcopter Vehicles. *'Computational aerodynamic modeling of small quadcopter vehicles,' AHS Forum 73*.

[7]   Huang, Y.B., Thomson, S.J., Hoffmann, W.C., Lan, Y.B., Fritz, B.K. (2013). Development and prospect of unmanned aerial vehicle technologies for agricultural production management. *International Journal of Agriculture and Biological Engineering*. vol. 6, no. 3, **DOI:10.3965/j.ijabe.20130603.001**.

[8]   Vorotović, G., Burazer, J., Bengin, A., Mitrović, Č., Januzović, M., Petrović, N., Novković, D. (2023). A Case Study of a Methodological Approach to the Verification of UAV Propeller Performance. *Strojniški vestnik - Journal of Mechanical Engineering*, vol. 69, no. 5-6, p. 199-207, **DOI:10.5545/sv-jme.2022.432**.

[9]   Gupte, S., Mohandas, P.I.T., Conrad, J.M. (2012). A survey of quadrotor unmanned aerial vehicles. *Proceedings of IEEE Southeast Con*, **DOI:10.1109/SECon.2012.6196930**.

[10] Brandt, J., Selig, M. (2020). Propeller performance data at low reynolds numbers. *AIAA Aerospace Sciences Meeting including the New Horizons Forum and Aerospace Exposition*, **DOI:10.2514/6.2011-1255**.

[11] Scanavino, M., Vilardi, A., Guglieri, G. (2020). An experimental analysis on propeller performance in a climate-controlled facility. *Journal of Intelligent & Robotic Systems*, vol. 100, p. 505-517, **DOI:10.1007/s10846-019-01132-9**.

[12] Russell, C., Jung, J., Willink, G., Glasner, B. (2016). Wind tunnel and hover performance test results for multicopter UAS vehicles. *AHS 72nd Annual Forum*.

[13] Abushahma, R.I.H., Ali, M.A.M., Rahman, N.A.A., Al-Sanjary, O.I. (2019). Comparative features of unmanned aerial vehicle (UAV) for border protection of Libya: A review. *IEEE 15th International Colloquium on Signal Processing & Its Applications*, p. 114-119, **DOI:10.1109/CSPA.2019.8695991**.

[14] Houghton, E.L., Carpenter, P.W. Collicott, S.H., Valentine, D.T. *Aerodynamics for Engineering Students: Seventh Edition*. Butterworth-Heinemann, Oxford.

[15] Liu, Y., Li, L., Ning, Z., Tian, W., Hu, H. (2018). Experimental investigation on the dynamic icing process over a rotating propeller model. *Journal of Propulsion and Power*, vol. 34, no. 4, p. 933-946, **DOI:10.2514/1.B36748**.

[16] Liu, Y., Li, L., Li, H., Hu, H. (2018). An experimental study of surface wettability effects on dynamic ice accretion process over an UAS propeller model. *Aerospace Science and Technology*, vol. 73, p. 164-172, **DOI:10.1016/j.ast.2017.12.003**.

[17] Han, N., Hu, H., Hu, H. (2021). An Experimental investigation on the dynamic ice accretion process over the blade surface of a rotating UAV propeller. *AIAA SCITECH Forum*, **DOI:10.2514/6.2022-1538**.

[18] Patel, Y. Gaurav, A., Srinivas, K., Singh, Y. (2017). A review on design and analysis of the propeller used in UAV. *International Journal of Advanced Production and Industrial Engineering*, vol. 605, p. 20-23.

[19] D. Kim, Y. Lee, S. Oh, Y. Park, J. Choi, D. Park, (2021). Aerodynamic analysis and static stability analysis of Manned/unmanned distributed propulsion aircrafts using actuator methods. *Journal of Wind Engineering and Industrial Aerodynamics*, vol. 214, art. ID 104648, **DOI:10.1016/j.jweia.2021.104648**.

[20] Kutty, H.A. Rajendran, P. (2017). 3D CFD simulation and experimental validation of small APC slow flyer propeller blade. *Aerospace*, vol. 4, no. 1, **DOI:10.3390/aerospace4010010**.

[21] Maalawi, K.Y., Badawy, M.T.S. (2001). A direct method for evaluating performance of horizontal axis wind turbines. *Renewable and Sustainable Energy Reviews*, vol. 5, no. 2, **DOI:10.1016/S1364-0321(00)00017-4**.

[22] Sartori, D. Yu, W. (2019). Experimental characterization of a propulsion system for multi-rotor UAVs. *Journal of Intelligent & Robotic Systems*, vol. 96, p. 529-540, **DOI:10.1007/s10846-019-00995-2**.

[23] Dahal, C., Dura, H.B., Poudel, L. (2021). Design and analysis of propeller for high-altitude search and rescue unmanned aerial vehicle. *International Journal of Aerospace Engineering*, art. ID 6629489, **DOI:10.1155/2021/6629489**.

[24] Ledoux, J., Riffo, S., Salomon, J. (2021). Analysis of the blade element momentum theory. *SIAM Journal of Applied Mathematic*, vol. 81, no. 6, **DOI:10.1137/20m133542x**.

[25] Yaakub, M.F., Wahab, A.A., Abdullah, A., Nik Mohd, N.A.R., Shamsuddin, S.S. (2017). Aerodynamic prediction of helicopter rotor in forward flight using blade element theory. *Journal of Mechanical Engineering and Science*, vol. 11, no. 2, p. 2711-2722, **DOI:10.15282/jmes.11.2.2017.12.0246**.